View metadata, citation and similar papers at core.ac.uk
brought to you by CORE
provided by CERN Document Server

THE SPEED AND ORIENTATION OF THE PARSEC-SCALE JET IN 3C 279

B. Glenn Piner[1], Stephen C. Unwin[2], Ann E. Wehrle[3], Alma C. Zook[4], C. Megan Urry[5], & Diane M. Gilmore[6]

ABSTRACT

A high degree of relativistic beaming is inferred for the jets of blazars based on several lines of evidence, but the intrinsic speed and angle of the jet to the line-of-sight for individual sources are difficult to measure. We have calculated inverse-Compton Doppler factors for 3C 279 using the collection of VLBI data (including high-resolution space VLBI data at low frequencies) recently published by us (as Wehrle et al. and Piner et al.), and the collection of multiwavelength spectra recently published by Hartman et al. From the Doppler factor and superluminal apparent speed, we then calculate the Lorentz factor and angle to the line-of-sight of the parsec-scale relativistic jet. We follow the method previously used by Unwin et al. for 3C 345 to model the jet components as homogeneous spheres and the VLBI core as an unresolved inhomogeneous conical jet, using Königl's formalism.

The conical-jet model can be made to match both the observed X-ray emission and the VLBI properties of the core with a suitable choice of Doppler factor, implying the core makes a significant contribution to the X-ray emission, in contrast to the situation for 3C 345, where the jet components dominated the X-ray emission. The parameters of the Königl models indicate the jet is particle dominated at the radii that produce significant emission (from ~ 5 to 20 pc from the apex of the jet for most models), and is not in equipartition. At the inner radius of the Königl jet the magnetic field is of order 0.1 G and the relativistic-particle number density is of order 10 cm^{-3}. The kinetic energy flux in the jet is of order $10^{46}(1+k)$ ergs sec^{-1}, where k is the ratio of proton to electron energy, which implies a mass accretion rate of order $0.1(1+k)/\eta M_\odot$ yr^{-1}, where η is the efficiency of conversion of mass to kinetic energy.

When all components are included in the calculation, then on average the core produces about half of the X-rays, with the other half being split between the long-lived component C4 and the brightest inner-jet component. We calculate an average speed and angle to the line-of-sight for the region of the jet interior to 1 mas of $v = 0.992c$ ($\gamma = 8$) and $\theta = 4°$, and an average speed and angle to the line-of-sight for C4 (at $r \approx 3$ mas) of $v = 0.997c$ ($\gamma = 13$) and $\theta = 2°$. These values imply average Doppler factors of $\delta = 12$ for the inner jet, and $\delta = 21$ for C4.

Subject headings: quasars: individual: (3C 279) — galaxies: jets — galaxies: active — radiation mechanisms: non-thermal — radio continuum: galaxies

1. INTRODUCTION

The quasar 3C 279 (z=0.536) has been one of the most intensively studied quasars for several reasons. It was the first radio source observed to exhibit the phenomenon of apparent superluminal motion (Knight et al. 1971; Whitney et al. 1971; Cohen et al. 1971), prompting continued study with VLBI through the 1970's and 1980's (Cotton et al. 1979; Unwin et al. 1989; Carrara et al. 1993) and 1990's (Wehrle et al. 2001; hereafter Paper I). A bright γ-ray flare was observed from 3C 279 in 1991 by the EGRET instrument shortly after the launch of the *Compton Gamma Ray Observatory* (Hartman et al. 1992), leading to a great deal of multiwavelength coverage during the following nine years. 3C 279 was one of the brightest γ-ray blazars detected during the lifetime of the EGRET instrument (Hartman et al. 1999). It is one of the prototypes for the class of luminous "red" blazars (Sambruna 2000).

These studies have produced a large amount of data on 3C 279. A number of nearly simultaneous multiwavelength spectra are available that show 3C 279 at various levels of activity. Data previously published by Maraschi et al. (1994), Hartman et al. (1996), and Wehrle et al. (1998) are compiled by Hartman et al. (2001a) (hereafter H01). Strong variability on timescales of a day or less has been observed in optical through γ-ray bands (e.g., Wehrle et al. 1998; Hartman et al. 2001b). In the radio regime, the variability timescale is longer, and flux density monitoring at 4.8, 8.4 and 14.5 GHz, complete with polarization data, has been obtained at the University of Michigan Radio Observatory (Aller et al. 1985). Monitoring at 22 and 37 GHz has been done at Metsähovi Observatory (Teräsranta et al. 1992, 1998). We have recently published a compendium of six years of VLBI images of 3C 279 at 22 and 43 GHz from 1991 to 1997 (Paper I), showing the kinematics of the parsec-scale jet. In this paper we combine the VLBI data

[1]Department of Physics and Astronomy, Whittier College, 13406 E. Philadelphia Street, Whittier, CA 90608; gpiner@whittier.edu

[2]Jet Propulsion Laboratory, Mail Code 301-486, 4800 Oak Grove Drive, Pasadena, CA 91109; Stephen.C.Unwin@jpl.nasa.gov

[3]Interferometry Science Center, California Institute of Technology, Mail Code 301-486, 4800 Oak Grove Drive, Pasadena, CA 91109; Ann.E.Wehrle@jpl.nasa.gov

[4]Department of Physics and Astronomy, Pomona College, Claremont, CA 91711; azook@pomona.edu

[5]Yale University, Physics Department, P.O. Box 208121, New Haven, CT 06520; meg.urry@yale.edu

[6]Space Telescope Science Institute, Science Comp. & Res. Support Div., 3700 San Martin Dr., Baltimore, MD 21218; dgilmore@stsci.edu

from Paper I with multiwavelength spectral information to calculate the Doppler factor, orientation, and speed of 3C 279's parsec-scale jet.

The two-humped overall spectral energy distribution of blazars is most naturally explained with a jet of relativistic electrons emitting a combination of synchrotron radiation for the radio through optical-uv region, and inverse-Compton emission at higher energies (e.g., Wehrle 1999). This interpretation of the spectrum leads to derivation of physical conditions in the jet that include bulk relativistic motion. Evidence for bulk relativistic motion in blazars comes from many sources, including the observed apparent superluminal motions in blazar jets (Vermeulen & Cohen 1994), the transparency of blazar cores to high-energy γ-rays (Dondi & Ghisellini 1995), rapid flux variability (Lähteenmäki & Valtaoja 1999), high VLBI core brightness temperatures (Tingay et al. 2001), an excess of predicted over observed inverse-Compton emission (Ghisellini et al. 1993), and arguments invoking equipartition or minimum energy requirements (Readhead 1994).

This bulk relativistic motion can be quantified by the ratio of observed to emitted frequency, or Doppler factor,

$$\delta = \frac{1}{\gamma(1 - \beta\cos\theta)}, \quad (1)$$

where θ is the angle to the line-of-sight, $\beta = v/c$, and $\gamma = (1-\beta^2)^{-1/2}$ is the bulk Lorentz factor. Although evidence for high values of δ is strong, calculating δ for any given source is difficult, as we explain below. Knowledge of δ is desirable because, together with the apparent superluminal speed, it constrains both the bulk Lorentz factor (important for studying jet energetics) and the angle of the jet to the line-of-sight (important for unification studies). One method of calculating the Doppler factor is to use source properties measured from VLBI images and multiwavelength spectra to predict the X-ray flux density that should be emitted by the Synchrotron Self-Compton (SSC) process. This calculation typically over-predicts the X-ray flux density from the source. By assuming the source is relativistically beamed with a certain δ (see equation (3)), the conflict between the predicted and the observed X-ray flux density can be eliminated (e.g., Marscher 1987; Ghisellini et al. 1993). If all of the X-rays from the source are not due to the SSC process from the component being considered, then a lower limit to δ is obtained rather than a firm value.

In practice, this method has many problems. It depends on the assumed geometry of the emitting region, and it depends sensitively on parameters that must be measured from multi-frequency VLBI images. Many authors assume a homogeneous sphere geometry for the VLBI core (e.g., Ghisellini et al. 1993; Mantovani et al. 2000). In reality, a homogeneous sphere is a poor approximation to the VLBI core, because it predicts a sharply-peaked synchrotron spectrum, and not the flat spectrum over several decades in frequency shown by many sources. A more realistic model for the VLBI core is an inhomogeneous conical jet, such as the model by Blandford & Königl (1979) and Königl (1981), which can reproduce the observed multiwavelength spectral indices. Estimates for parameters such as the synchrotron turnover frequency of VLBI components also bring uncertainty into this calculation, and Lähteenmäki, Valtaoja, & Wiik (1999) show that plotting SSC Doppler factors derived by various authors from different data sets for the same sources results in an almost pure scatter diagram, most likely due to varying assumptions about input parameters.

SSC Doppler factors have been calculated in detail perhaps only for 3C 345 by Unwin et al. (1994, 1997). They modeled 3C 345 as a superposition of an inhomogeneous conical jet (using Königl's 1981 formalism) for the VLBI core, and a series of homogeneous spheres for the VLBI components or "blobs". They then used multi-frequency VLBI data, quasi-simultaneous X-ray data, and the multiwavelength spectrum to constrain the Doppler factor of 3C 345. In this paper, we apply the procedure used by Unwin et al. (1994, 1997) for obtaining inverse-Compton Doppler factors to 3C 279.

Note that our goal in this paper is not to model the entire multiwavelength spectrum and short-term variability of 3C 279 using the Königl model. We use the Königl model as a geometry somewhat more sophisticated than a homogeneous sphere to calculate what we hope will be an accurate measurement of the SSC Doppler factor, in order to constrain the jet orientation and speed. In particular, we make no effort to model the γ-ray portion of the spectrum, because models including other radiation mechanisms, such as that of H01 and Ballo et al. (2002), show that this is quite likely due to external Compton scattering and not SSC. The model of H01 does indicate that the lower energy portion of the inverse-Compton spectrum (the X-rays) is likely to be dominated by SSC emission. We also consider only the comparatively "quiescent" emission from 3C 279, because the rapid variability during flares may originate in components much smaller than the Königl jet, presumably small blobs (like those in the H01 model) that are moving out through the inhomogeneous jet and are superposed with the VLBI core in the VLBI images (see Paper I). Note that even sophisticated homogeneous models such as that of H01 do not come close to fitting the radio emission, showing that some form of inhomogeneous jet component is required.

While X-ray emission on larger scales in blazar jets may be caused by inverse-Compton scattering of the microwave background (e.g., Celotti, Ghisellini, & Chiaberge 2001), on the parsec scales considered in this paper the synchrotron photon energy density is orders of magnitude higher than the microwave background energy density (about 10^{-4} ergs cm^{-3} compared to 10^{-10} ergs cm^{-3}, using expressions from Celotti et al. 2001). Because of this large difference in energy densities, inverse-Compton scattering of the microwave background is not considered further in this paper.

2. OBSERVATIONS

The VLBI data used for this paper are taken from the 22 and 43 GHz VLBI observations of 3C 279 presented in Paper I. These data included 18 epochs spanning the time range from 1991 to 1997 (at 22 GHz) and 1995 to 1997 (at 43 GHz). Earlier epochs in this sequence used the Global VLBI Network and Mark II recording, later epochs used the NRAO VLBA telescopes and correlator. The reader is referred to Paper I for further discussion of the VLBI observations, and the VLBI images, model fits, and component identifications. Two mosaics at 22 and 43 GHz

from that paper are shown in Figures 1 and 2 for ease in identifying features. Throughout the rest of this paper, C4 refers to the moving component approximately three milliarcseconds from the core, C5 refers to the stationary component at one milliarcsecond from the core, and C5a, C6, C7, C7a, C8, and C9 refer to the moving components that sequentially emerge from the core during the course of the monitoring. See Paper I for more details. High resolution VLBI data at low frequencies is needed to constrain the optically thick VLBI component spectral indices, so we also make use of the 1.6 and 5 GHz space VLBI (VSOP) observations of 3C 279 from Piner et al. (2000).

Multiwavelength spectra of 3C 279 are needed to constrain inputs to both the homogeneous sphere and inhomogeneous jet models. For this purpose, we use the set of contemporaneous multiwavelength spectra compiled by H01. Eleven such spectra spanning the years 1991 to 2000 are presented in that paper. We fit these spectra using four broken power laws applied to the different regions of the spectrum, to provide the appropriate inputs to the models. Table 1 lists our power-law fits to the multiwavelength spectra of H01, for epochs from 1991 to 1997. We exclude H01's epochs P3a (which has no X-ray data) and P5b (the very large flare from 1996 February). Spectral indices follow the naming convention of Königl (1981): α_{s1} is the optically thick synchrotron spectral index below the turnover frequency, α_{s2} is the synchrotron spectral index above the turnover frequency but below the break frequency, α_{s3} is the synchrotron spectral index above the synchrotron break frequency, and α_{c2} is the inverse-Compton spectral index in the X-ray region of the spectrum. The sign convention for spectral indices in this paper is $S \propto \nu^{+\alpha}$. Errors on the fitted spectral indices were calculated from the errors in the measured flux densities given in H01. When only one X-ray measurement was available at a given epoch in H01, the X-ray spectral index was acquired from the original X-ray paper referenced by H01. Table 1 also gives the fitted turnover frequency and flux density at the turnover frequency (ν_t and S_t), the fitted break frequency and flux density at the break frequency (ν_b and S_b), and a reference X-ray measurement specified by ν_x and S_x that we attempt to match with the models. Figure 3 shows the power-law fits to the spectra from Table 1.

3. CALCULATION OF SSC DOPPLER FACTORS

The VLBI morphology and multiwavelength data cannot be adequately explained by either an inhomogeneous jet (§ 3.2) or a homogeneous sphere (or spheres) model (§ 3.1) alone. In a combined model (§ 3.3), we require the Doppler factor to be the same for the jet and spheres; the spheres can therefore be regarded as approximations to dense clumps propagating along with the bulk jet.

3.1. *Homogeneous Sphere Model*

Possibly the two simplest blazar models are the homogeneous sphere model (Gould 1979) and the inhomogeneous jet (Blandford and Königl 1979; Königl 1981). In both models, the source is assumed to be moving relativistically at a small angle to the line-of-sight, and the electrons responsible for the synchrotron emission have a power-law distribution in energy. As implied by their names, the homogeneous sphere model assumes that the photon density within the spherical source is uniform, while the inhomogeneous jet model assumes that the source is a conical jet in which the magnetic field and electron number density have power-law dependences on the distance from the apex of the jet.

The homogeneous sphere model, the simpler of the two, requires six observables to determine the Doppler factor and the angle between the source velocity and the line-of-sight. Three of these characterize the synchrotron spectrum: the spectral index of the optically thin spectrum, and the flux density and frequency at which the sphere first becomes optically thick (the "turnover" flux density and frequency). Adding the angular size should in principle determine the entire spectrum of the source, if the X-rays are the result of SSC scattering of the synchrotron photons. In practice, such a calculation predicts X-ray flux densities that are several orders of magnitude larger than observed, if the bulk motion of the source is assumed to be non-relativistic. This "Compton catastrophe" can be avoided if the source has a relativistic bulk velocity, and in this case the observed X-ray flux density (the fifth observable) provides a constraint that determines the Doppler factor. Together with the apparent superluminal speed (the sixth observable), this determines both the bulk velocity and the angle to the line-of-sight.

Figure 4 shows sample homogeneous sphere spectra plotted with five-frequency VLBI data from late 1997 and early 1998. The data at 15, 22, and 43 GHz are from the VLBA observation on 1997 Nov 16 (Paper I), while the data at 1.6 and 5 GHz are from the VSOP observation on 1998 January 9 (Piner et al. 2000). The three brightest components in the source at that epoch (the core, the long-lived bright component C4, and the newly emerged components C8/9, blended except at 43 GHz) are plotted on this figure. Homogeneous sphere spectra are calculated from

$$S(\nu) = S_0(\nu_t/\nu_0)^{\alpha}(\nu/\nu_t)^{2.5}(1 - e^{-\tau}), \qquad (2)$$

where ν_t is the turnover frequency, α is the optically thin spectral index, S_0 is the flux density at frequency ν_0, and $\tau = (\nu_t/\nu)^{2.5-\alpha}$. The sphere spectra have been adjusted to go through the three highest frequency observations for each component. Inspection of Figure 4 shows that homogeneous spheres cannot fit the spectra of either the core or the jet components. This is because a homogeneous sphere has an optically thick spectral index of 2.5, while the actual components have optically thick indices much less than this (~ 1.0). Evidently there are inhomogeneities in the "components" that broaden the self-absorption turnover and cause the spectral index below the turnover to be less than 2.5. The high-resolution space VLBI data at low-frequencies was crucial to obtaining this result; ground-based images at low frequencies blend the components so a spectral dissection like that in Figure 4 cannot be obtained. The primary advantage of the homogeneous sphere model is its simplicity; it requires a minimum number of observables to constrain the Doppler factor. For this reason, we proceed with the homogeneous sphere calculation in this section, with the expectation that corrections due to inhomogeneities (at least for the jet components) will be small. An alternative geometry for the VLBI core (a conical jet) is tried in the next subsection. An alternative geometry for jet components (oblique shocks) is considered by, e.g., Aller et al. (2001).

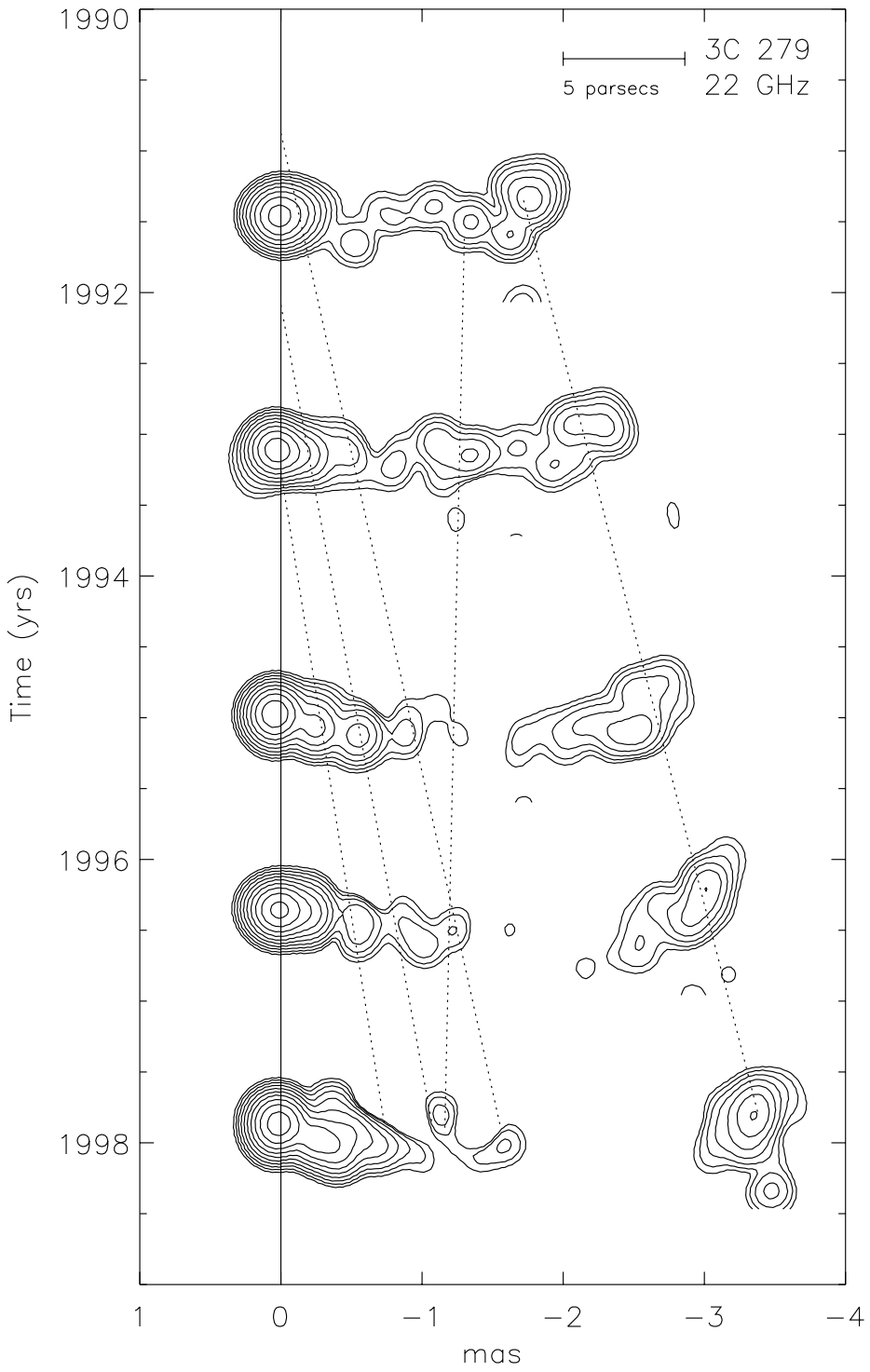

FIG. 1.— Time-series mosaic of a selection of 22 GHz VLBI images of 3C 279. Epochs 1991 Jun 24, 1993 Feb 17, 1994 Sep 21, 1996 May 13, and 1997 Nov 16 are shown. The images have been restored with a circular 0.2 mas beam without residuals and rotated 25° counterclockwise. The lowest contour is 25 mJy beam^{-1}; subsequent contours are a factor of two higher than the previous contour. The solid line indicates the position of the presumed stationary core. The dotted lines represent the best fits to the model-fit Gaussian positions vs. time. From right to left these lines represent C4, C5, C5a, C6, and C7. Some lines have been extended before and after model-fit detections to show speculative zero-separation epochs and later positions.

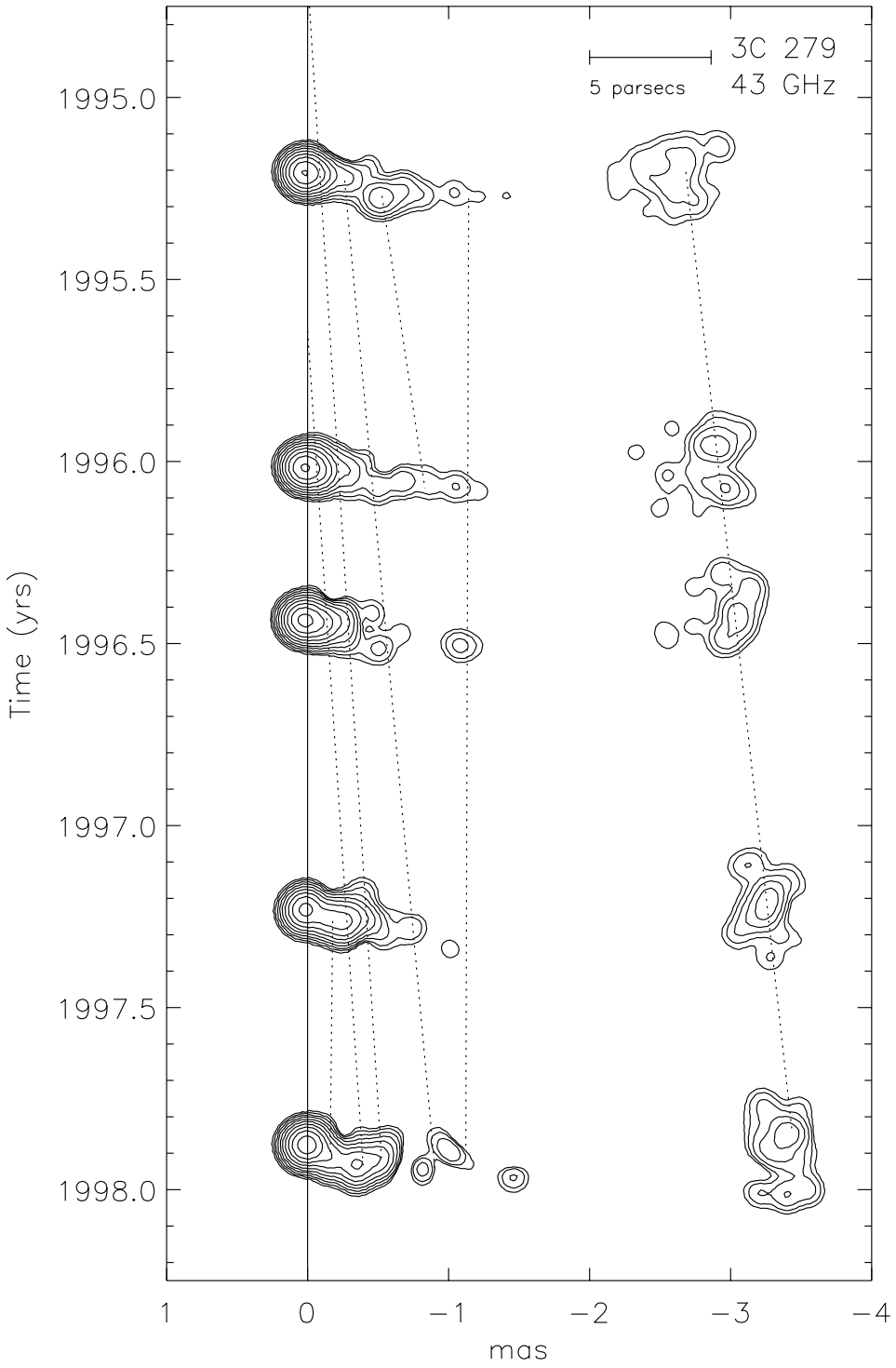

FIG. 2.— Time-series mosaic of a selection of 43 GHz VLBI images of 3C 279. Epochs 1995 Mar 19, 1996 Jan 7, 1996 Jun 9, 1997 Mar 29, and 1997 Nov 16 are shown. The images have been restored with a circular 0.15 mas beam without residuals and rotated 25° counterclockwise. The lowest contour is 25 mJy beam^{-1}; subsequent contours are a factor of two higher than the previous contour. The solid line indicates the position of the presumed stationary core. The dotted lines represent the best fits to the model-fit Gaussian positions vs. time. From right to left these lines represent C4, C5, C6, C7, C7a, C8, and C9. Some lines have been extended before model-fit detections to show speculative zero-separation epochs.

TABLE 1

SPECTRAL INDICES AND BREAKPOINTS DERIVED FROM MULTIWAVELENGTH CAMPAIGN DATA, AND REFERENCE X-RAY MEASUREMENTS

Date Range	Epoch†	$\alpha_{s1}^{\ddagger}$	$\alpha_{s2}^{\ddagger}$	$\alpha_{s3}^{\ddagger}$	$\alpha_{c2}^{\ddagger}$	ν_t^* (Hz)	S_t^* (Jy)	$\nu_b^{\diamond}$ (Hz)	$S_b^{\diamond}$ (Jy)	ν_x° (keV)	S_x° (μJy)
1991 Jun 15 — 1991 Jun 28	P1	0.22 ± 0.01	-0.57 ± 0.05	-1.29 ± 0.06	-0.67 ± 0.03	$6.8 \pm^{0.5}_{0.5} \times 10^{10}$	$18.6 \pm^{0.5}_{0.5}$	$1.1 \pm^{0.5}_{0.3} \times 10^{13}$	$1.0 \pm^{0.5}_{0.3}$	10.0	0.90
1992 Dec 22 — 1993 Jan 12	P2	0.24 ± 0.02	-0.81 ± 0.03	-1.66 ± 0.03	-0.91 ± 0.07	$6.5 \pm^{0.3}_{0.3} \times 10^{10}$	$20.3 \pm^{0.5}_{0.5}$	$1.8 \pm^{0.4}_{0.4} \times 10^{13}$	$0.21 \pm^{0.08}_{0.05}$	1.0	1.00
1993 Dec 13 — 1994 Jan 3	P3b	0.33 ± 0.02	-0.59 ± 0.07	-1.28 ± 0.03	-0.75 ± 0.17	$5.9 \pm^{0.5}_{0.4} \times 10^{10}$	$27.3 \pm^{1.0}_{0.9}$	$2.1 \pm^{0.8}_{0.6} \times 10^{12}$	$3.4 \pm^{1.3}_{0.9}$	2.3	0.62
1994 Nov 29 — 1995 Jan 10	P4	0.22 ± 0.01	-0.63 ± 0.05	-1.61 ± 0.17	-0.65 ± 0.11	$4.2 \pm^{0.2}_{0.2} \times 10^{10}$	$21.2 \pm^{0.5}_{0.5}$	$5.2 \pm^{5.0}_{2.6} \times 10^{12}$	$1.0 \pm^{0.8}_{0.5}$	2.4	0.49
1996 Jan 16 — 1996 Jan 30	P5a	0.33 ± 0.03	-0.50 ± 0.12	-1.72 ± 0.10	-0.66 ± 0.02	$5.7 \pm^{1.4}_{1.1} \times 10^{10}$	$26.5 \pm^{2.2}_{2.0}$	$1.1 \pm^{0.8}_{0.5} \times 10^{13}$	$1.9 \pm^{1.8}_{0.9}$	10.0	0.33
1996 Dec 10 — 1997 Jan 28	P6a	0.33 ± 0.03	-0.73 ± 0.08	-1.53 ± 0.07	-0.67 ± 0.02	$4.2 \pm^{0.3}_{0.3} \times 10^{10}$	$28.9 \pm^{1.0}_{0.9}$	$1.4 \pm^{1.0}_{0.6} \times 10^{13}$	$0.43 \pm^{0.44}_{0.22}$	9.5	0.23
1997 Jun 17 — 1997 Jun 24	P6b	0.39 ± 0.01	-0.73 ± 0.06	-1.99 ± 0.20	-0.70 ± 0.10	$4.3 \pm^{0.2}_{0.2} \times 10^{10}$	$33.8 \pm^{0.8}_{0.8}$	$8.3 \pm^{4.4}_{2.9} \times 10^{13}$	$0.14 \pm^{0.11}_{0.07}$	3.0	0.48

† Epoch identification in H01.

‡ α_{s1} is the optically thick synchrotron spectral index below the turnover frequency, α_{s2} is the synchrotron spectral index above the turnover frequency but below the break frequency, α_{s3} is the synchrotron spectral index above the synchrotron break frequency, and α_{c2} is the inverse-Compton spectral index in the X-ray region of the spectrum.

$*$ ν_t and S_t are the fitted synchrotron turnover frequency and flux density at the turnover frequency.

$\diamond$ ν_b and S_b are the fitted synchrotron break frequency and flux density at the break frequency.

$\circ$ ν_x and S_x are the frequency and flux density of the reference X-ray measurement.

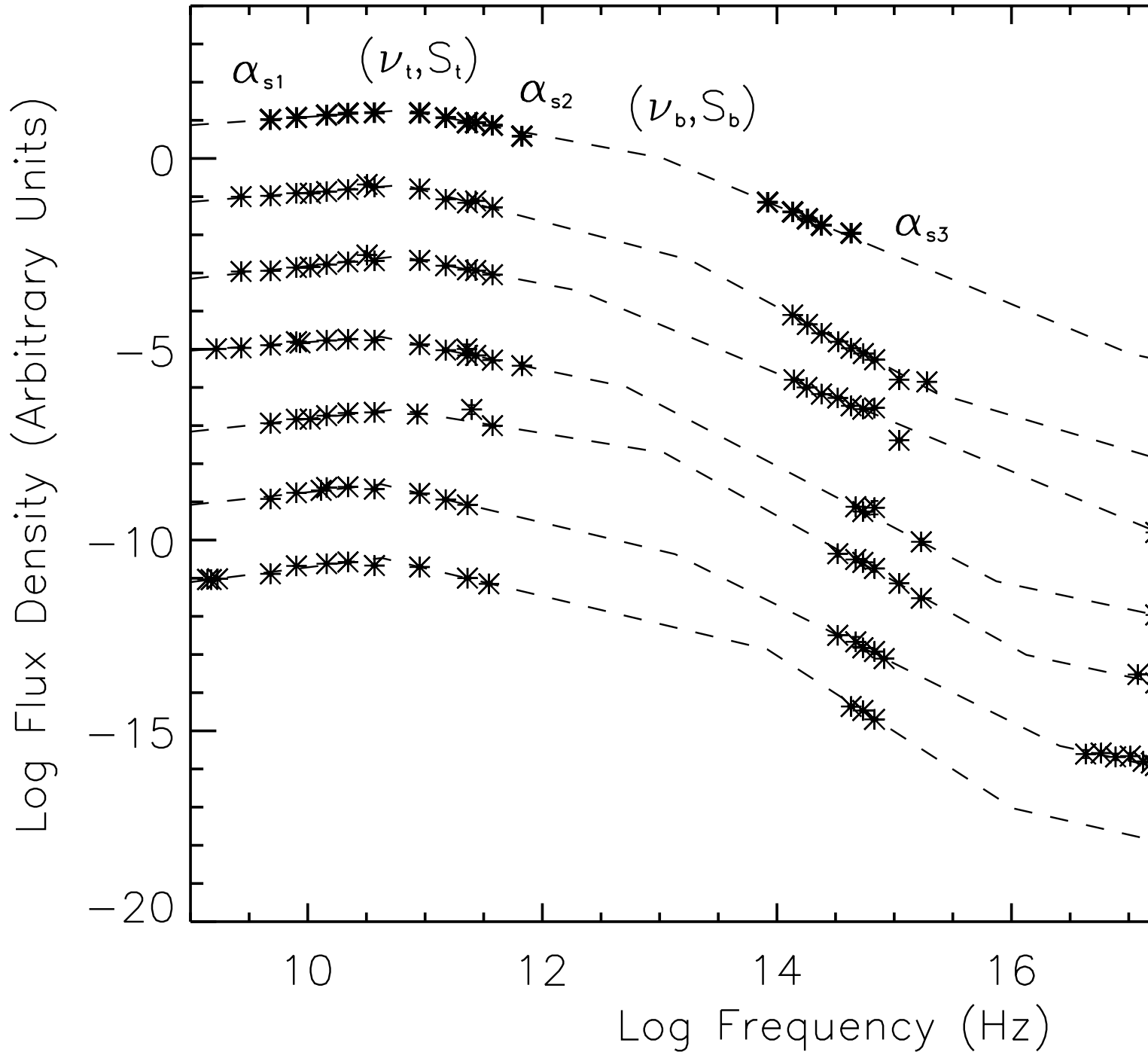

FIG. 3.— Fits of the multiwavelength spectra from Table 1 with four power laws. The flux density scale in Janskys is correct for the top (P1) spectrum, after that each successive spectrum is offset by two orders of magnitude in flux density. The error bars are smaller than the plotting symbols. The parameters of the fits are given in Table 1, and the epoch designations from Table 1 are listed to the right of the figure. The spectral indices and breakpoints are labeled for the P1 spectrum.

The Doppler factor of a homogeneous sphere that produces SSC X-rays of flux density S_x Jy at frequency ν_x (in keV) is (Ghisellini et al. 1993):

$$\delta = f(\alpha) S_t \left[\frac{\ln(\nu_b/\nu_t)\nu_x^\alpha}{S_x \xi_d^{6-4\alpha} \nu_t^{5-3\alpha}} \right]^{1/(4-2\alpha)} (1+z), \qquad (3)$$

where $f(\alpha) \approx -0.08\alpha + 0.14$, S_t is the flux density (in Jy) at the turnover frequency ν_t (in GHz) obtained by extrapolating the straight-line optically thin slope (Marscher 1987), ν_b is the synchrotron break frequency in GHz, ξ_d is the angular diameter of the VLBI component (in mas), and α is the optically thin spectral index. Equation (3) finds the Doppler factor for which the given spherical component produces all the X-ray flux density from the source. Since the other components must also contribute X-rays at some level, the Doppler factor found by this method is a lower limit for the given component. To put this method into practice to find an actual Doppler factor for 3C 279, we must assume the source has a constant Doppler fac-

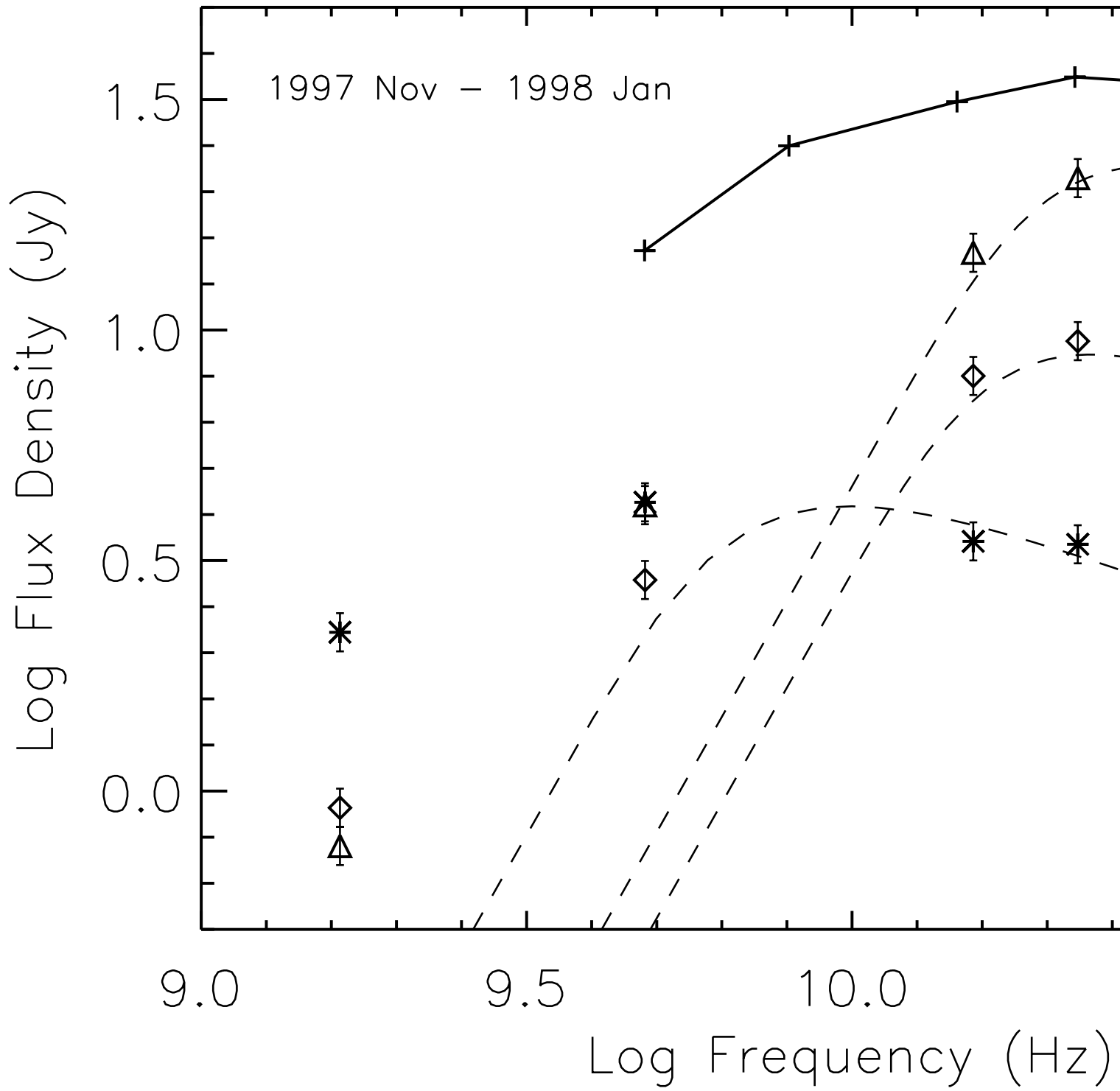

FIG. 4.— Five-frequency VLBI spectra of 3C 279 core and jet components from observations between 1997 November and 1998 January. Three bright components are shown: the VLBI core (triangles), the blended component C8/9 (diamonds), and C4 (asterisks). The single-dish spectrum from Michigan and Metsähovi monitoring is also shown (plus signs). Three sample homogeneous sphere spectra that match the three highest frequencies for each component are also shown.

tor along its jet. We then apply equation (3) to find the lower limit to the Doppler factor for each component at a given epoch. The actual Doppler factor at that epoch must then be somewhat larger than the highest lower limit found from equation (3). We then calculate the Doppler factor that will produce the observed X-ray flux density from the sum of the X-rays from all components, and what percentage of the observed X-ray flux density is produced by each component.

In Table 2 we show the inputs to equation (3) and the resulting Doppler factor lower limits at each 22 GHz VLBI epoch, for those components found to produce a significant percentage ($> 1\%$) of the X-ray flux density at that epoch. The parsec-scale radio structure of 3C 279 consists of the

TABLE 2
LOWER LIMITS TO THE DOPPLER FACTOR COMPUTED USING THE HOMOGENEOUS SPHERE MODEL

VLBI Epoch	H01 Epoch	Comp.	S_t (Jy)	ν_t (GHz)	α	ξ_d (mas)	δ
1991 Jun 24	P1 (1991 Jun 15 — 1991 Jun 28)	C4	4.1	7.0	-0.5	0.25	15.7
1992 Jun 14	P2 (1992 Dec 22 — 1993 Jan 12)	Core	20.5	65.0	-0.81	0.20	5.9
		C4	4.4	7.0	-0.5	0.49	7.3
1992 Nov 10	P2 (1992 Dec 22 — 1993 Jan 12)	Core	18.6	65.0	-0.81	0.14	10.0
		C6	4.4	22.2	-0.6	0.25	4.2
		C4	6.2	7.0	-0.5	0.83	4.4
1993 Feb 17	P2 (1992 Dec 22 — 1993 Jan 12)	Core	22.7	65.0	-0.81	0.16	9.1
		C4	5.2	7.0	-0.5	0.79	4.0
1993 Nov 8	P3b (1993 Dec 13 — 1994 Jan 3)	Core	24.7	58.7	-0.59	0.16	11.8
1994 Mar 2	P3b (1993 Dec 13 — 1994 Jan 3)	Core	23.5	58.7	-0.59	0.14	13.8
		C7	6.7	22.2	-0.6	0.20	8.7
1994 Jun 12	P4 (1994 Nov 29 — 1995 Jan 10)	Core	28.0	42.4	-0.63	0.18	18.7
1994 Sep 21	P4 (1994 Nov 29 — 1995 Jan 10)	Core	26.2	42.4	-0.63	0.18	17.5
1995 Jan 4	P4 (1994 Nov 29 — 1995 Jan 10)	Core	21.8	42.4	-0.63	0.13	25.9
1995 Feb 25	P4 (1994 Nov 29 — 1995 Jan 10)	Core	17.6	42.4	-0.63	0.16	14.0
		C7	3.1	22.2	-0.6	0.11	11.8
1995 Mar 19	P4 (1994 Nov 29 — 1995 Jan 10)	Core	22.7	42.4	-0.63	0.14	21.8
1996 Jan 7	P5a (1996 Jan 16 — 1996 Jan 30)	Core	23.2	56.6	-0.5	0.11	26.1
		C4	4.2	7.0	-0.5	0.40	9.6
1996 May 13	P5a (1996 Jan 16 — 1996 Jan 30)	Core	24.3	56.6	-0.5	0.11	27.2
		C7a/C8	8.7	22.2	-0.6	0.20	11.4
1996 Jun 9	P5a (1996 Jan 16 — 1996 Jan 30)	Core	25.3	56.6	-0.5	0.07	54.4
1997 Jan 15	P6a (1996 Dec 10 — 1997 Jan 28)	Core	26.2	42.4	-0.73	0.12	30.1
		C8	14.5	22.2	-0.6	0.22	17.9
		C4	6.6	7.0	-0.5	0.31	24.6
1997 Mar 29	P6a (1996 Dec 10 — 1997 Jan 28)	Core	20.7	42.4	-0.73	0.10	31.0
		C8/9	16.1	22.2	-0.6	0.18	26.8
		C4	4.6	7.0	-0.5	0.20	34.5
1997 Jul 16	P6b (1997 Jun 17 — 1997 Jun 24)	Core	24.8	42.8	-0.73	0.13	26.8
		C8/9	16.9	22.2	-0.6	0.31	12.4
		C4	7.8	7.0	-0.5	0.43	17.0
1997 Nov 16	P6b (1997 Jun 17 — 1997 Jun 24)	Core	41.4	42.8	-0.73	0.14	38.1
		C4	8.9	7.0	-0.5	0.40	22.3

compact core, the bright long-lived component C4 located about 3 mas from the core at these epochs, and a series of short-lived inner-jet components that have all faded by the time they reached about 1 mas from the core. The inner-jet components have similar spectra, typified by the spectra of the blended component C8/9 in Figure 4. We use C8/9 as a guide for all of the inner-jet components, and take them to have $\nu_t = 22$ GHz and $\alpha = -0.6$ (see Figure 4). For component C4, we take $\nu_t = 7$ GHz and $\alpha = -0.5$, based on power-law fits to the optically thick and thin portions of the spectrum in Figure 4. For the core turnover frequency and spectral index, we use the turnover frequency and spectral index (α_{s2}) of the multiwavelength spectrum from the H01 epoch closest in time to the VLBI epoch (see Table 1), since the core dominates the high-radio-frequency spectrum. S_t for the jet components is calculated from the observed flux density at the turnover frequency (for the inner-jet components), or extrapolated to 7 GHz (for C4), with the opacity correction described by Marscher (1987) applied ($S_t = S_{obs}e^{\tau_m}$), where τ_m is tabulated by Marscher (1987). The core S_t is taken to be the greater of S_t from the closest multiwavelength spectrum with extrapolations of jet component flux densities subtracted, or the observed 22 GHz (or 43 GHz if available) VLBI core flux density with the opacity correction applied. ξ_d is taken to be the VLBI model-fit size (or size upper limit if the fitted size is zero), multiplied by 1.8 to convert from the model fit Gaussian FWHM to the diameter of an optically thin sphere (Pearson 1995). ν_b, ν_x, and S_x are taken from Table 1, from the multiwavelength spectrum closest in time to the VLBI epoch. Note equation (3) is very insensitive to these three values (e.g., $\delta \propto S_x^{0.2}$ for $\alpha = -0.5$), X-ray variability between the X-ray and VLBI observation should not have a large affect (e.g., if the X-ray flux density increases by a factor of 10, the calculated Doppler factor increases by a factor of 1.6).

In Table 3 we calculate the Doppler factor for each epoch, assuming that all components at a given epoch have the same Doppler factor, and that the total X-ray emission from all components must equal the observed X-

Table 3
X-Ray Production in the Homogeneous Sphere Model

		Fraction of Total X-Rays by Component						
Epoch	δ	Core	C4	C6	C7	C7a/C8†	C8	C8/9†
1991 Jun 24	16	...	1.00	...	...	...	...	...
1992 Jun 14	8	0.22	0.78	...	...	...	...	...
1992 Nov 10	10	0.97	0.02	0.01	...	...	...	...
1993 Feb 17	9	0.98	0.02	...	...	...	...	...
1993 Nov 8	12	1.00	...	...	...	...	...	...
1994 Mar 2	14	0.92	...	...	0.08	...	...	...
1994 Jun 12	19	1.00	...	...	...	...	...	...
1994 Sep 21	18	1.00	...	...	...	...	...	...
1995 Jan 4	26	1.00	...	...	...	...	...	...
1995 Feb 25	15	0.71	...	...	0.29	...	...	...
1995 Mar 19	22	1.00	...	...	...	...	...	...
1996 Jan 7	26	0.99	0.01	...	...	...	...	...
1996 May 13	27	0.99	...	...	...	0.01	...	...
1996 Jun 9	54	1.00	...	...	...	...	...	...
1997 Jan 15	32	0.69	0.26	...	...	...	0.05	...
1997 Mar 29	39	0.30	0.55	...	...	...	...	0.15
1997 Jul 16	27	0.89	0.09	...	...	...	...	0.02
1997 Nov 16	39	0.94	0.06	...	...	...	...	...

† Refers to a blended component.

ray emission. This Doppler factor will be at least slightly higher than the highest lower limit found for that epoch in Table 2, since each lower limit in Table 2 assumed the component under consideration was the sole source of the X-ray emission. Errors in the turnover frequency and angular size in equation (3) cause large errors in the calculated Doppler factor ($\delta \propto \nu_t^{1.3}$ and $\xi_d^{1.6}$ for $\alpha = -0.5$). Because our measurements of these quantities are only accurate to about 25%, we estimate our calculated Doppler factor lower limits in Tables 2 and 3 to be correct only to within a factor of two. The Doppler factor values listed in Table 3 confirm this: the average Doppler factor is 23, and the measured values show about a factor of two scatter around this value, with most falling between 10 and 40. There is some indication that the Doppler factor increases with time from 1991 to 1997, but given the errors in the calculated Doppler factor, this may not be significant. The calculated relative X-ray brightness of components in turn depends on the Doppler factor from Table 3 to a high power ($S_x \propto \delta^5$ for $\alpha = -0.5$), so the relative X-ray brightnesses of components can be in error by as much as a factor of 30. This means that any of the components listed as producing more than several percent of the X-ray emission at a given epoch in Table 3 is a candidate for producing most of the X-rays. At eight of the epochs listed in Table 3, the calculations show that the core produces at least two orders of magnitude more X-rays than the next brightest component, and the calculations show the core to be the leading X-ray producer at 15 of the 18 epochs. Despite the large errors in the calculations, we can conclude that in the homogeneous sphere model, the VLBI core is the dominant source of the X-ray emission from late 1992 through 1997. It appears that C4 dominated the X-ray emission for a time prior to 1992 (due to its small size at that time), and that there may also be contributions at about the 10% level from whatever inner-jet component has just emerged from the core (this changes from C6 to C9 over the course of the observations).

3.2. *Inhomogeneous Conical Jet Model for Core*

In this subsection we consider an alternate geometry for the VLBI core, the inhomogeneous jet model of Königl (1981). The jet is represented by a cone with opening half-angle ϕ, and the axis of the jet makes an angle θ with the line-of-sight ($\theta > \phi$). The bulk Lorentz factor of the jet is γ, the electron Lorentz factor is γ_e. Electron Lorentz factors lie between the limits γ_{el} and γ_{eu}, where γ_{el} is set to 100 for all models. The magnetic field and electron number density (or electrons plus positrons) are determined by $B = B_1 r^{-m}$ and $n_e(\gamma_e) = K_e r^{-n} \gamma_e^{(2\alpha_e - 1)}$, where r is the distance in parsecs from the apex of the jet, $\alpha_e = \alpha$ and $K_e = K1$ for $\gamma_e < \gamma_{eb}$, and $\alpha_e = \alpha - 0.5$ and $K_e = K1\gamma_{eb}$ for $\gamma_e > \gamma_{eb}$, where γ_{eb} is a function of r ($\gamma_{el} < \gamma_{eb} < \gamma_{eu}$). The location of the break in the power-law is estimated by equating the jet travel time to a distance r with the synchrotron cooling time; see equation (4) of Königl (1981) and equation (21) of Blandford & Königl (1979). The VLBI 'core' emission is then due to the integrated spectrum of the unresolved conical jet, and the position and size of the core change with frequency in a predictable way. At low frequencies, the dominant emission region follows the local turnover frequency and moves in with increasing frequency ($r \propto \nu^{-1/k_m}$, where $k_m = ((3-2\alpha)m+2n-2)/(5-2\alpha)$), and the spectral index of the integrated spectrum is α_{s1}. At radius r_M and frequency ν_t, the local break frequency becomes less than the

TABLE 4
FITTED VALUES OF CONICAL-JET SPECTRAL PARAMETERS

Epoch	α	m	n	α_{s1}	α_{s2}	α_{s3}	α_{c2}	k_m
P1	-0.4	1.6	1.5	0.21	-0.66	-1.31	-0.57	1.2
P2	-0.6	2.0	0.8	0.18	-0.85	-1.60	-0.68	1.3
P3b	-0.3	1.8	1.5	0.33	-0.55	-1.28	-0.46	1.3
P4	-0.4	1.7	1.4	0.22	-0.65	-1.35	-0.55	1.3
P5a	-0.5	2.0	1.1	0.30	-0.78	-1.45	-0.62	1.4
P6a	-0.5	1.9	1.3	0.34	-0.81	-1.37	-0.66	1.4
P6b	-0.5	1.9	1.4	0.39	-0.84	-1.32	-0.68	1.4

turnover frequency, and the dominant emission region begins to follow the local break frequency and moves out with increasing frequency ($r \propto \nu^{1/k_b}$, where $k_b = 3m-2$), until $\gamma_{eb} = \gamma_{eu}$ at frequency ν_b and radius $r = (\nu_b/\nu_t)^{1/k_b} r_M$, which we set to be r_u, the upper radius of the Königl jet. We use this set of conditions to determine γ_{eu} in our models. The spectral index of the integrated spectrum in this region is α_{s2}. Above ν_b, the dominant emission region moves in with frequency, following the increasing magnetic field ($r \propto \nu^{-1/m}$), and the integrated synchrotron spectrum falls with index α_{s3}. We extend the calculated emission from the upper synchrotron branch interior to r_M, and that from the lower synchrotron branch exterior to r_u, rather than truncating the spectrum at these radii as Königl does. The reader is referred to Hutter & Mufson (1986) for an illuminating diagram of this model in the radius vs. frequency plane.

3.2.1. *Calculation of α, m, and n*

The parameters α, m, and n completely determine the synchrotron and SSC spectral indices of the integrated spectrum by the following equations (Königl 1981):

$$\alpha_{s1} = \frac{-15 + 4\alpha + 5m - 4\alpha m + 5n}{3m - 2\alpha m + 2n - 2} \tag{4}$$

$$\alpha_{s2} = \max \begin{bmatrix} \frac{4\alpha m - 2\alpha - m - n + 3}{3m-2} \\ \alpha - 0.5 \end{bmatrix} \tag{5}$$

$$\alpha_{s3} = -(m + 2 - n)/m \tag{6}$$

$$\alpha_{c1} = \min \begin{bmatrix} \frac{-4\alpha m - 2\alpha n + 6\alpha + 5m + 10n - 20}{3m - 2\alpha m + 2n - 2} \\ 1 \end{bmatrix} \tag{7}$$

$$\alpha_{c2} = \alpha - \frac{(1-\alpha)m + 2n - 4}{7m - 4} \tag{8}$$

The SSC index α_{c1} (associated with the optically thick portion of the synchrotron spectrum) is not observable in the multiwavelength spectrum because the SSC emission in this frequency range lies well below the synchrotron emission. The SSC index α_{c2} (associated with the optically thin portion of the synchrotron spectrum) is the SSC index that is actually observed in the X-ray portion of the multiwavelength spectrum.

Since the Königl model parameters are so closely tied to the multiwavelength spectrum, we make one calculation of δ for each multiwavelength epoch listed in Table 1, rather than one for each VLBI epoch as in § 3.1. We fit values of α, m, and n at each epoch by finding the combination that most closely reproduces the four observable spectral indices, given in Table 1 for each multiwavelength epoch. We take into account the errors on the observed spectral indices given in Table 1, and find the values of α, m, and n that minimize χ^2 at each epoch.

Fitted values of α, m, and n are given in Table 4, along with the spectral indices calculated from these best-fit values, for comparison with Table 1. In some cases, only modest agreement could be made with some of the observed indices. Note that the observed α_{s1} is an integrated value for the source that includes some steep-spectrum jet emission. The observed α_{s1} is therefore a only limiting value for the core α_{s1}, and later we modify the fits so the radio emission from the Königl model lies slightly below the total observed radio emission. The magnetic field index m is restricted to lie between 1 (for a purely transverse field) and 2 (for a purely longitudinal field). Fitted values for α lie between -0.3 and -0.6, those for m between 1.6 and 2.0, and those for n between 0.8 and 1.5. In Table 4 we also give Königl's parameter k_m that controls the frequency dependent size of the core, which is proportional to ν^{-1/k_m}. This provides an independent check on the model fits, and using the mean core sizes at 22 and 43 GHz from Paper I we calculate a k_m of 1.2, in good agreement with the mean k_m of 1.3 from Table 4.

3.2.2. *Calculation of Jet Doppler Factor*

The fitted values of α, m, and n from Table 4, along with other observable parameters, were used as inputs to a Königl model calculation at each epoch, implemented in the Mathcad software package. The other input parameters were: the synchrotron turnover frequency and flux density and the synchrotron break frequency from Table 1, the observed superluminal speed, and the projected distance of the VLBI core from the apex of the jet, r_{proj}. The angle of the jet to the line-of-sight was then varied until the predicted X-ray flux density from the Königl jet, including both synchrotron and SSC flux density, matched the observed X-ray flux density S_x at frequency ν_x from Table 1. Once the angle to the line-of-sight is known, the observed superluminal speed then determines the intrinsic jet speed and Doppler factor, and the opening half-angle of the jet ϕ can be calculated from equations in Königl (1981).

Table 5
Results from Conical-Jet Model Fits

Epoch*	r_{proj} (mas)	ϕ_{app} (deg)	ξ_r (mas)	θ (deg)	γ	δ	r_M (pc)	r_u (pc)	$B^\dagger$ (G)	$n_e{}^\dagger$ (cm^{-3})	$U_e/U_B(r_M)^\ddagger$	$U_e/U_B(r_u)^\ddagger$
P1	0.27	11.6	0.055	14.0	5.5	4.0	2.6	15.8	0.23	42	5.1	338
P1*	0.18	14.4	0.045	11.8	5.3	4.9	1.5	7.7	0.30	73	4.8	234
P2	0.28	11.8	0.058	6.5	5.8	8.1	6.3	25.7	0.17	5.5	0.9	168
P2*	0.19	13.6	0.045	4.9	6.3	9.8	4.1	15.2	0.22	9.7	0.9	122
P3b	0.21	13.2	0.048	3.3	7.3	12.3	10.1	28.8	0.17	1.3	0.3	6
P3b*	0.16	11.7	0.033	2.6	8.1	14.3	7.4	18.6	0.21	3.3	0.4	7
P4	0.31	10.9	0.059	10.0	5.3	5.7	6.2	29.1	0.16	4.2	0.8	142
P4*	0.22	11.4	0.044	7.8	5.5	7.0	4.0	16.7	0.21	8.5	1.1	51
P5a	0.36	9.4	0.059	7.8	5.5	7.1	7.8	29.0	0.14	7.6	2.0	223
P5a*	0.23	12.9	0.051	6.3	5.8	8.3	4.5	15.1	0.19	12	1.7	126
P6a	0.50	7.6	0.066	10.0	5.3	5.7	10.4	49.4	0.12	6.8	2.7	343
P6a*	0.31	10.5	0.057	8.2	5.5	6.8	5.8	24.8	0.16	11	2.2	205
P6b	0.45	8.4	0.066	5.1	6.2	9.5	18.4	143	0.10	1.5	0.7	323
P6b*	0.28	10.9	0.053	3.5	7.2	12.1	12.6	87.2	0.14	2.0	0.5	173

*Models indicated by an asterisk have ν_t increased by a factor of 1.5 and S_t decreased by a factor of 0.75 relative to their values in Table 1. This allows for some emission from the extended jet, which causes the core radio flux density to lie slightly below the observed single-dish radio flux density.

†Magnetic field and total electron number density are evaluated at radius r_M.

‡Ratio of electron to magnetic energy density at r_M and r_u.

Input parameters not taken from Table 1 were determined as follows. The superluminal speed was taken to be the measured speed of the inner-jet components C6, C7, C7a, and C8 (the components closest to the core during the relevant epochs) from Paper I. Measured speeds of these four components are consistent with a constant average inner-jet speed of $5.2c$ (see Table 4 of Paper I), which was the apparent speed adopted for these model fits. The projected distance of the VLBI core from the apex of the jet, r_{proj}, is not a directly observable quantity, but does effect two observable quantities: the measured core radius $\xi_r \approx r_{proj} \sin\phi / \sin\theta$, and the apparent jet opening angle $\phi_{app} \approx \phi / \sin\theta$. In practice, r_{proj} was varied until the best fit was obtained to the observed values of these two quantities: $\xi_r = 0.059 \pm 0.018$ mas (using the mean FWHM of the Gaussian model fits from Paper I, and multiplying by 1.6 to convert to the diameter of an optically thick sphere [Pearson 1995]), and $\phi_{app} = 10.5 \pm 5.3^\circ$ (using the mean opening angle given by component C4 from Paper I, with C4's Gaussian FWHM converted to the diameter of an optically thin sphere for consistency).

Results from this model fitting, including the adopted value of r_{proj} and the calculated values of ϕ_{app}, ξ_r, θ, δ, and γ, are given in Table 5. Also given in Table 5 are r_M (the smallest radius from which synchrotron emission with index α is observed), r_u (in our implementation, the largest radius from which synchrotron emission with index $\alpha - 0.5$ is observed), the magnetic field and relativistic-particle number density at r_M, and the ratio of relativistic particle to magnetic energy density at r_M and r_u. A sketch of a sample geometry from Table 5 is shown in Figure 5. The model synchrotron and SSC spectra are shown in Figure 6, where the sums of these spectra are compared with the observed multiwavelength spectra.

In reality, some of the radio emission from 3C 279 is due to the parsec-scale jet that is resolved by VLBI observations, and not to the partially resolved core. To take this into account, we constructed an alternate set of model fits with ν_t increased by a factor of 1.5 and S_t decreased by a factor of 0.75 (relative to their values in Table 1). This causes the predicted core radio flux density to lie slightly below the observed single-dish radio flux densities, allowing for some emission from the extended jet (Piner et al. 2000; de Pater & Perley 1983), which does not contribute significantly to the integrated spectrum above the turnover frequency. In these models the jet contributes ~ 3 Jy at 5 GHz, and these model fits are indicated by an asterisk next to the epoch name in Table 5. This set of models is used in all subsequent calculations.

The agreement between the calculated and observed spectra is reasonably good, although there are discrepancies (particularly with the optical flux densities, e.g., 1994 Nov 29 — 1995 Jan 10, period P4 in H01) of about a factor of 2. There are several reasons for this: the optical flux density of 3C 279 is known to vary by as much as 60% on timescales of a day (Balonek & Kartaltepe 2002) so variability may be a factor, in some cases one of the four observed spectral indices was poorly matched by the three free parameters α, m, and n, and at some epochs there are apparently significant synchrotron X-rays, so the observed α_{c2} is not an accurate measurement of the Compton spectral index at those epochs. The spectra in Figure 6 do not extend up to the EGRET energy range, and we do not attempt to model the high-energy γ-ray emission with the Königl model. Although the Königl model can produce γ-rays in the EGRET energy range, there is considerable

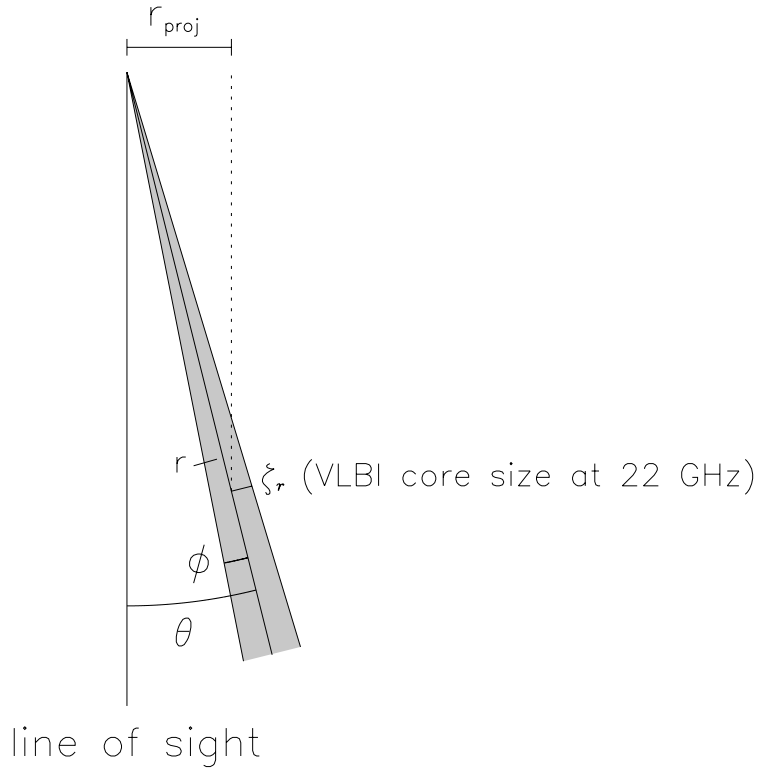

FIG. 5.— Geometry of the conical-jet model, with numerical values taken from the first row of Table 5 (the fit to the 1991 Jun 15 — 1991 Jun 28 (P1) epoch). Note that ϕ is the opening half-angle of the jet, ξ_r is the jet cross-sectional radius, r is the linear distance along the jet, and r_{proj} is the projected linear distance along the jet.

evidence that the GeV emission is external Compton and not SSC (Kubo et al. 1998; H01; Ballo et al. 2002), so we do not apply the EGRET data as a constraint on our SSC model.

The values of the Doppler factor obtained by applying a conical geometry to the core are about a factor of two lower than the Doppler factors obtained using a spherical geometry (§ 3.1), showing that the assumed geometry can have a moderate influence on the SSC Doppler factor. The average Doppler factor from the fits in Table 5 that allow for emission from an extended jet is 9 with a scatter of ±3. When inputs to the model are all varied by 10% (such that the changes all act together to increase or decrease the Doppler factor), the fitted δ can be made to vary by about 30%. Thus variations in the Doppler factor from epoch to epoch in Table 5 could be due to the observational uncertainties in the input parameters, rather than real variations in the Doppler factor.

3.3. *Combined Conical-Jet/Sphere Models*

We are now in a position to make a model for the source that combines the conical VLBI core with the homogeneous sphere VLBI jet components (§ 3.1). We use the homogeneous sphere values from Table 2, and the conical-jet core values from Table 5, using the multiwavelength epoch closest in time to each VLBI epoch. As in § 3.1, each calculated Doppler factor (either conical jet or sphere) provides a lower limit to the Doppler factor at that epoch (assuming a constant Doppler factor along the jet), since each calculation assumes the component under consideration produces all of the X-rays. We solve for *one* Doppler factor at each epoch as follows. We lower the X-ray flux density attributed to the conical-jet core in the Königl-jet fitting program, while adjusting r_{proj} to maintain the observed values of ϕ_{app} and ξ_r. This has the effect of raising the calculated Doppler factor. We use this Doppler factor to calculate the X-ray flux density that would be observed from the jet components in Table 2, and add these flux densities to that attributed to the VLBI core. We continue this process until we find a total X-ray flux density that equals the observed X-ray flux density. Results of this process are given in Table 6. The parameter space of the Königl jet model is complicated, and there is not a simple relation between the observed X-ray flux density and δ as for the homogeneous sphere. In most regions of parameter space δ is a slowly varying function of the X-ray flux density as for a sphere, but there are regions where δ can change dramatically in response to a small change in the X-ray flux density (e.g., the last two entries in Table 6, where, as the solution for θ begins to approach zero, the Lorentz factor increases to maintain the observed superluminal speed, producing the high Doppler factors in these models).

We reiterate that the predicted X-ray emission depends strongly on the observed quantities, so that any of the components listed as producing more than several percent

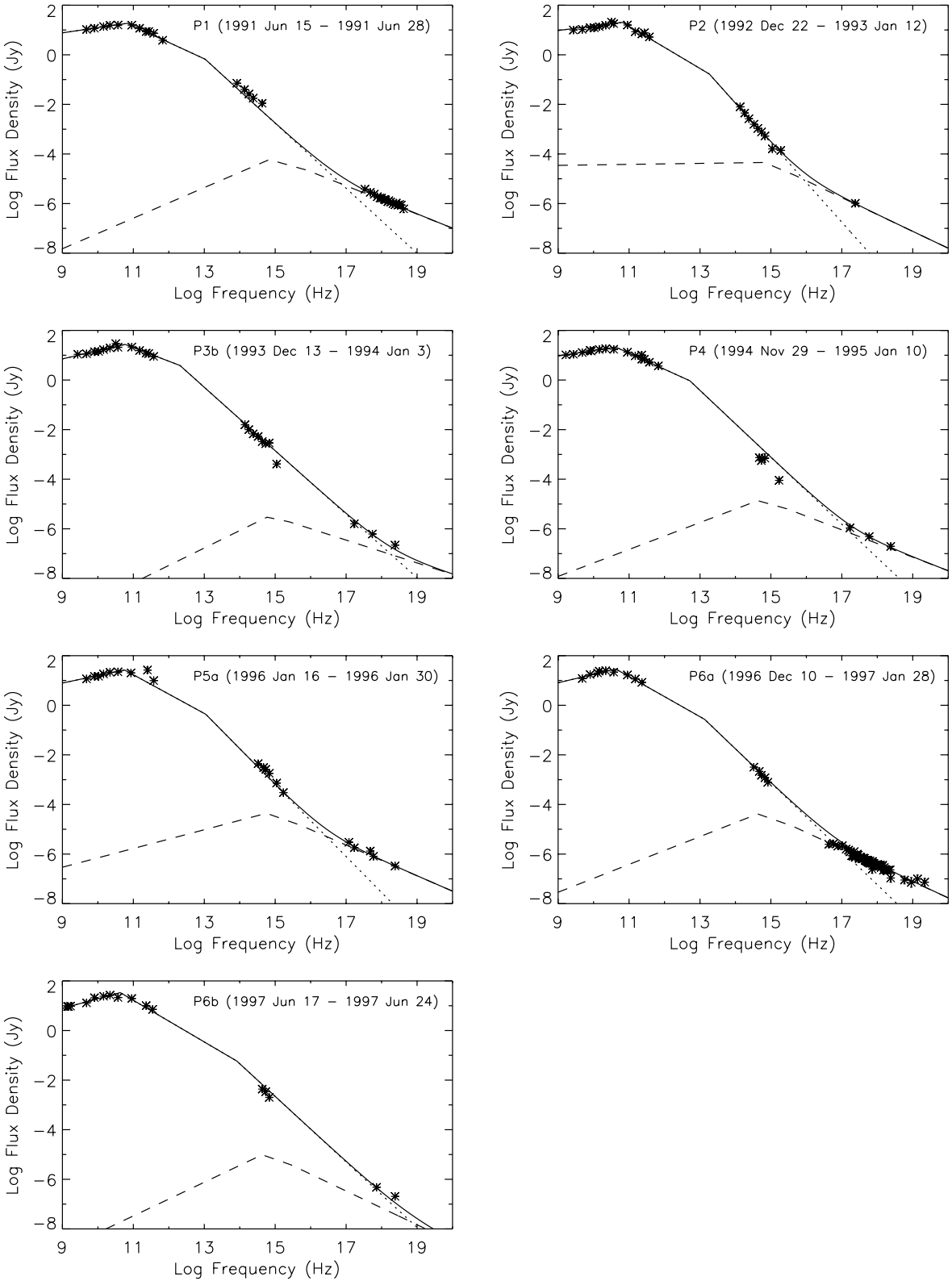

FIG. 6.— Sum of the calculated synchrotron and inverse-Compton spectra from the Königl model fit to each multiwavelength epoch, compared with the observed flux densities at each multiwavelength epoch, indicated by asterisks. The spectral sum is indicated by the solid line, the synchrotron spectrum by the dotted line, and the inverse-Compton spectrum by the dashed line.

Table 6
X-Ray Production in the Combined Conical-Jet/Sphere Model

		Fraction of Total X-Rays by Component								$\theta^{\ddagger}$	
Epoch	δ	Core	C4	C6	C6/7†	C7	C7a/C8†	C8	C8/9†	(deg)	$\gamma^{\ddagger}$
1991 Jun 24	16	0.09	0.91	...	...	...	...	...	...	2.8	9.8
1992 Jun 14	10	0.83	0.17	...	...	...	...	...	...	4.4	6.6
1992 Nov 10	10	0.97	0.02	0.01	...	...	...	...	...	4.8	6.4
1993 Feb 17	10	0.99	0.01	...	...	...	...	...	...	4.9	6.3
1993 Nov 8	14	1.00	...	...	...	...	...	...	...	2.6	8.1
1994 Mar 2	15	0.95	...	...	...	0.05	...	...	...	2.3	8.6
1994 Jun 12	8	0.77	0.15	...	...	0.08	...	...	...	6.6	5.7
1994 Sep 21	8	0.84	0.01	...	0.15	...	...	...	...	6.9	5.7
1995 Jan 4	8	0.72	0.07	0.05	...	0.16	...	...	...	6.3	5.8
1995 Feb 25	13	0.36	0.01	...	...	0.63	...	...	...	3.2	7.4
1995 Mar 19	9	0.57	0.06	...	...	0.37	...	...	...	5.3	6.1
1996 Jan 7	11	0.48	0.51	...	...	...	0.01	...	...	4.9	8.1
1996 May 13	12	0.28	0.16	...	...	...	0.56	...	...	3.4	7.2
1996 Jun 9	19	0.08	0.18	...	...	...	0.74	...	...	1.6	10.2
1997 Jan 15	26	0.08	0.77	...	...	...	...	0.15	...	1.2	14.1
1997 Mar 29	37	0.09	0.72	...	...	...	...	...	0.19	0.6	19.3
1997 Jul 16	27	0.87	0.11	...	...	...	...	...	0.02	0.8	13.8
1997 Nov 16	33	0.85	0.15	...	...	...	...	...	...	0.5	16.8

† Refers to a blended component.
‡ These values are discussed in § 4.2.4.

of the X-ray emission at a given epoch in Table 6 is a candidate for producing most of the X-rays. Because of this, it is better to consider averages over many epochs than the entry in Table 6 from a single epoch. On average, modeling the core as a conical jet rather than a homogeneous sphere reduces its contribution to the X-ray flux density. When the core is modeled as a conical jet, then on average the core produces about half of the X-rays, with the other half being split about evenly between C4 and the brightest inner-jet component.

4. DISCUSSION

4.1. *Comparison to Other Estimates of δ for 3C 279*

A strong lower limit to the Doppler factor can be obtained by enforcing the condition that the emitting region should be transparent to γ-rays. Inferring a source size from the γ-ray variability timescale during the large flare in early 1996, Wehrle et al. (1998) find $\delta > 6.3$ for 1 GeV photons and $\delta > 8.5$ for 10 GeV photons. This agrees very well with the lower limit to the core δ found at this epoch in this paper, $\delta > 8.3$ (Table 5), and with the overall δ found at this epoch, δ=11 (Table 6).

An independent method for measuring δ is to compare the radio core brightness temperatures measured from VLBI maps and from radio light curves (Lähteenmäki et al. 1999). Since these depend on the intrinsic brightness temperature multiplied by δ raised to different powers, a measured value of δ can be extracted from these two observables. We applied this method to 3C 279 in Paper I and found δ=7.4 at epoch 1995.2. Again, this agrees very well with the lower limit to the core δ found at this epoch in this paper, $\delta > 7.0$ (Table 5), and with the overall δ found at this epoch, δ=9 (Table 6). The similar Doppler factors found from these two independent methods differ from the much higher Doppler factor ($\delta \sim 100$) found when equipartition between magnetic and particle energy is assumed (Paper I). Other calculations of an equipartition Doppler factor for 3C 279 (e.g. Güijosa & Daly 1996) have found a lower equipartition Doppler factor because they did not have access to the high-resolution (and high brightness temperature sensitivity) VLBI data presented in Paper I.

Models using various emission processes and geometries to explain the multiwavelength spectra of 3C 279, including the γ-ray emission, have constrained δ as part of their model fitting. Some examples are as follows: Maraschi, Ghisellini, & Celotti (1992) used an accelerating parabolic jet where δ varied from 10 to 18. Ghisellini & Madau (1996) assumed δ=14 for application of their "mirror" model to the high-energy emission of 3C 279. H01 and Ballo et al. (2002) find Doppler factors ranging from 8 to 23 and from 12 to 19 respectively for application of their models to the various multiwavelength spectra presented in those papers. In these cases the angle to the line-of-sight and/or the Lorentz factor are assumed input quantities, so the derived Doppler factors are merely consistent within the framework of the particular model, not actual Doppler factor measurements. In addition, these models do not apply constraints from the VLBI observations as we do in this paper, so they predict features in the VLBI maps that are not observed. The models mentioned in this paragraph predict apparent speeds in the inner jet ranging from 1 to 24c, whereas the observations show apparent

speeds in the inner jet to be about $5c$ (Paper I), which is enforced by all of the models in Table 5.

Note that our reliance on the apparent superluminal speed assumes that the pattern speed observed in the VLBI observations (Paper I) is equal to the bulk fluid speed. While there is one stationary component (C5) that clearly does not move at the bulk fluid speed, all five components observed in the inner jet of 3C 279 (C5a, C6, C7, C7a, and C8) during the course of the monitoring described in Paper I moved with approximately the same apparent speed of $5c$, so we take this value as an indicator of the apparent fluid speed in the inner jet. If the apparent speed is not used as an observable, then the speed and orientation of the jet are not tightly constrained in our models. For example, allowing the apparent bulk speed to range from 1 to $10c$ allows the following ranges of parameters for the P1 model in Table 5: $5^\circ < \theta < 14^\circ$, $3 < \gamma < 24$, and $2 < \delta < 4$.

4.2. *Implications of Königl Jet Model*

4.2.1. *Comparison to Sphere Model Results*

In comparing conical and spherical models for the VLBI core, we find that a smaller Doppler factor is required to reduce the predicted core X-ray flux density to the measured X-ray flux density using the conical geometry. This implies that, if a conical geometry is indeed the correct geometry for the VLBI core, inverse-Compton calculations such as those of Ghisellini et al. (1993) that have assumed a spherical geometry may have systematically overestimated δ in their samples.

4.2.2. *Implications of α, m, and n*

The values of α, m, and n derived for the Königl model determine the orientation of the magnetic field and the ratio of relativistic particle to magnetic energy density. The value of m can vary between 1 and 2 in the Königl model, with $m = 1$ corresponding to a purely transverse magnetic field, and $m = 2$ to a purely longitudinal field. Conservation of particle number in a conical jet requires that $n = 2$, our values of $n < 2$ imply that the total number of relativistic particles increases down the jet (e.g., from continuous acceleration adding to the total number of relativistic electrons). Our fitted values of α vary between -0.3 and -0.6, our values of n between 0.8 and 1.5, and our values of m between 1.6 and 2.0, which corresponds to a predominantly longitudinal magnetic field in the region of the jet modeled by the Königl model, which is about 0.1 mas in size for 3C 279. In contrast, VLBI polarimetry observations at many frequencies from 15 to 86 GHz (Leppänen, Zensus, & Diamond 1995; Taylor 1998; Lister, Marscher, & Gear 1998; Homan & Wardle 1999; Lister & Smith 2000; Attridge 2001) have given magnetic field vectors oriented perpendicular to the jet in the core region. We do not consider these results to be in conflict, since the VLBI polarimetry observations show the core to have low levels of polarization even at 86 GHz (Attridge 2001), suggestive of an initially tangled field that becomes ordered at shocks outside the Königl jet region. VLBI polarimetry with beams smaller than 0.1 mas would be needed to image the magnetic field structure in the region modeled in this paper.

The values of m and n also determine how the ratio of relativistic particle to magnetic energy density varies along the jet (it goes approximately as r^{-n+2m}), this ratio is quoted in Table 5 at radii r_M and r_u. The jet is close to equipartition at r_M, but the degree of particle dominance increases down the jet, and at r_u the relativistic-particle energy density dominates the magnetic energy density by roughly two orders of magnitude. The increasing particle dominance of Königl jets with jet radius seems to be a common feature of these models when n and m are determined from spectral fits (rather than assumed). Similar particle dominance was found by Unwin et al. (1994, 1997) and by Hutter and Mufson (1986), who attributed the result qualitatively to a conversion of magnetic energy to particle energy by magnetohydrodynamic jet acceleration. If the Königl model is a correct description of the VLBI core of 3C 279, then this core is not in equipartition, which could explain why 3C 279's equipartition Doppler factor is so much higher than the Doppler factor measurements obtained by other means (see § 4.1). This finding contrasts with that of Lähteenmäki et al. (1999), who find that Doppler factors computed by comparing variability and VLBI brightness temperatures in general agree with equipartition Doppler factors, although analysis of brightness temperature measurements from the high-resolution VLBI data of Paper I has shown that this is not the case for 3C 279.

From the particle energy density, we can calculate the energy flux associated with the particles from

$$L_{kin} \approx \frac{4}{3}\pi c r_{jet}^2 \gamma^2 U_e (1+k), \tag{9}$$

where r_{jet} is the linear size of the jet cross-sectional radius, U_e is the relativistic-particle energy density (see Table 5), and k is the ratio of proton to electron energy. See De Young (2002) equation (4.107), Bicknell (1994) equation (52), and Celotti & Fabian (1993) equation (1) for discussions of this equation. Note that U_e depends on γ_{el}, which is not precisely known (although the observed lack of Faraday rotation in most extragalactic radio sources implies $\gamma_{el} > 100$, Jones & O'Dell 1977), so that this is only an order-of-magnitude calculation. From equation 9, the particle energy flux is of order $10^{46}(1+k)$ ergs s^{-1}. This is of the same order as the particle kinetic energy fluxes found by Celotti & Fabian (1993), for a sample of sources that included 3C 279. The particle energy flux is about an order of magnitude higher than the bolometric radiative luminosity of 3C 279's jet (Hartman et al. 1996) after correction for beaming, which falls within the range of L_{kin}/L_{rad} found by Celotti & Fabian (1993). An energy flux of $10^{46}(1+k)$ ergs s^{-1} is equivalent to an energy injection rate of order $0.1(1+k)M_\odot$ yr^{-1}, or a mass accretion rate of order $0.1(1+k)/\eta M_\odot$ yr^{-1}, where η is the efficiency of conversion of mass to kinetic energy.

We can compare the values of α, m, and n found here for 3C 279 with values of these parameters found for other sources where the Königl model has been applied. The source apart from 3C 279 with the most constraints from spectral and VLBI data is 3C 345. Unwin et al. (1994) found $\alpha = -0.6$, $m = 1.5$, and $n = 1.4$ for 3C 345 in mid-1990. Unwin et al. (1997) found $\alpha = -0.6$, $m = 1.9$, and $n = 1.7$ for 3C 345 in mid-1992, and at this epoch they found that the Königl-jet core was not the dominant X-ray emitter in the source. Hutter & Mufson (1986) found

$1.1 < m < 1.6$ and $1.1 < n < 1.6$ with an assumed α of -0.5 in their application of the Königl model to three nearby BL Lac objects.

4.2.3. *Need for an additional homogeneous component*

The spectral index in the Königl model fit for 3C 279 that has the poorest observational constraints is the synchrotron index below the turnover frequency, α_{s1}. This is because the extended jet emits a significant fraction of the flux at low radio frequencies, so that what we get from the single-dish spectra shown in Figure 6 is the spectrum of the core plus jet, when what we want is the spectrum of the core alone. The observed α_{s1} thus provides only a limit to the actual α_{s1}, with high-resolution VLBI at low frequencies being needed to accurately measure α_{s1}. There are indications from VSOP observations at 1.6 and 5 GHz (Piner et al. 2000) that, at least at that epoch, the spectral index of the VLBI core was much more inverted than the values of α_{s1} quoted in Table 1. If confirmed by further VSOP data on 3C 279 (Edwards et al. in preparation), this would rule out a pure Königl jet model for the 3C 279 core at these epochs. Because the Königl model was created in part to explain the flat radio spectra of quasars, very inverted values of α_{s1} (less than about -1.0) create contradictions in the model, such as a synchrotron break that goes the 'wrong way' ($\alpha_{s3} > \alpha_{s2}$). This situation could be rectified by adding a homogeneous component (a newly emerging 'blob') that is blended with the VLBI core on the VLBI images.

It seems likely that, in the general case, the spectrum of the VLBI core is a blend of an inhomogeneous component like a Königl jet and one or more shocks moving along the jet. Because these would all be merged on the VLBI images, it would be impossible to determine an inverse-Compton Doppler factor in this case, because the crucial observational constraint provided by the VLBI size would be missing. The degree to which the "quiescent" emission from 3C 279 can be represented by a single inhomogeneous component will determine the reliability of the Doppler factors computed from the conical-jet geometry.

4.2.4. *Speed and Orientation of the Jet*

The Lorentz factor γ and angle to the line-of-sight θ of the jet can be calculated if δ and the apparent speed β_{app} are known:

$$\gamma = \frac{\beta_{app}^2 + \delta^2 + 1}{2\delta} \tag{10}$$

and

$$\theta = \arctan \frac{2\beta_{app}}{\beta_{app}^2 + \delta^2 - 1}. \tag{11}$$

In their similar work on 3C 345, Unwin et al. (1997) calculate the jet speed and angle to the line-of-sight at several radii along the jet. This was possible for 3C 345 because the jet component C7 was the only good candidate for producing the X-ray emission, so the inverse-Compton Doppler factor measured for C7 (assuming C7 produced 100% of the X-rays) could be combined with the apparent speed measured for C7 at different points along the jet to produce a plot of γ and θ vs. r (see Figure 4 of Unwin et al. 1997).

The situation for 3C 279 is not so straightforward. As discussed in § 3.3, the core, inner-jet components, and C4 all probably contribute a non-negligible fraction of the X-ray emission. A unique solution for δ for each component can only be obtained by knowing *a priori* what this fraction is. Table 5 gives Lorentz factors and angles to the line-of-sight for the conical-jet core under the assumption that the core produces all of the X-rays. Average values of γ and θ obtained in this fashion are $\gamma = 6$ and $\theta = 6°$. Better estimates of γ and θ can be obtained by using instead the Doppler factor that reproduces the observed X-ray emission when *all* components are considered (see Table 6). This provides a reasonable estimate for γ and θ for the component listed as producing the majority of the X-ray emission at that epoch. These values of γ and θ are listed in the final two columns of Table 6. At epochs where the core or an inner-jet component was the dominant X-ray producer we used the average apparent speed of the inner jet of $5.2c$. At the 4 epochs where C4 was the dominant X-ray producer we used the apparent speed of C4, or $7.5c$ (Paper I). In this fashion, we obtained average Lorentz factors and angles to the line-of-sight for the core and inner-jet region ($r < 1$ mas) of $\gamma = 8$ and $\theta = 4°$, and an average Lorentz factor and angle to the line-of-sight for C4 (at $r \approx 3$ mas) of $\gamma = 13$ and $\theta = 2°$. These numbers apply only for a specific portion of C4's curved trajectory (see below), along this portion of its trajectory C4 is faster, in intrinsic speed and apparent speed, and its path is closer to the line-of-sight than the inner jet components.

Whether this speed and angle are characteristic of C4's location in the jet or are unique to C4 is unknown, because all components other than C4 faded by the time they reached 1 mas from the core during the period of our monitoring (see Paper I for a discussion). The quoted speed and angle for C4 apply for times when C4 was contributing significantly to the X-ray emission, at the beginning and the end of the observed time range. The Doppler factor of C4 is evidently time-variable and increased around 1997, coincident with its brightening on the component light curves (Paper I). In Paper I we presented a detailed analysis of the kinematics of C4, based on its curved trajectory in the VLBI images. For that analysis we assumed $\gamma = 13$ (slightly higher than the minimum γ required for the maximum apparent speed along C4's curved path). We confirm this choice of γ in this paper, and also confirm the other results from the kinematic analysis in Paper I: that the angle to the line-of-sight of C4 is about 2°, and that C4's Doppler factor was highest at the beginning and end of the observed time range (see Figure 8 of Paper I).

5. CONCLUSIONS

In this paper we have calculated, as accurately as is possible, inverse-Compton Doppler factors for 3C 279. These Doppler factors were then used to compute the speed and orientation of the parsec-scale jet. Calculation of inverse-Compton Doppler factors is a notoriously inaccurate business. Nevertheless, given the large amount of multiwavelength spectral data recently published by H01, and the large amount of VLBI data recently published by us (Paper I), 3C 279 seems to be the best object for constraining the Doppler factor by this method. Progress on this calculation for other sources is hindered mainly by the reliance on the turnover frequency of the core and jet components, which is a critical parameter that is relatively poorly constrained observationally, even for this well-observed source

(see Figure 4). Nearly simultaneous VLBI observations at as many frequencies as possible (and as near as possible to the same resolution) are required before attempting such a calculation.

Major conclusions from this work are:

1. The VLBI morphology and multiwavelength data cannot be adequately explained by either an inhomogeneous jet (§ 3.2) or a homogeneous sphere (or spheres) geometry (§ 3.1) alone. We have used a combined model (§ 3.3), where we assume an inhomogeneous conical-jet geometry for the VLBI core and a homogeneous sphere geometry for the VLBI components. In this combined model, we require the Doppler factor to be the same for the jet and spheres; the spheres can therefore be regarded as approximations to dense clumps propagating along with the bulk jet. By applying this method, we obtain an average speed and angle to the line-of-sight for the core and inner-jet region ($r < 1$ mas) of $v = 0.992c$ ($\gamma = 8$) and $\theta = 4°$, and an average speed and angle to the line-of-sight for C4 (at $r \approx 3$ mas) of $v = 0.997c$ ($\gamma = 13$) and $\theta = 2°$.

2. When the core is modeled as a conical jet, then on average the core produces about half of the X-rays, with the other half being split about evenly between C4 and the brightest inner-jet component. This result differs from that for 3C 345 found by Unwin et al. (1997), who could not match the Königl model to 3C 345's X-ray emission, and concluded the core is not the dominant X-ray emitter in 3C 345.

3. The jet is particle dominated at most radii that produce significant observed emission in the Königl model. This result was also found by Unwin et al. (1994) for 3C 345. At the inner radius of the Königl jet the magnetic field is of order 0.1 G and the relativistic-particle number density is of order 10 cm^{-3}. The kinetic energy flux in the jet is of order $10^{46}(1+k)$ ergs sec^{-1}, where k is the ratio of proton to electron energy, which implies a mass accretion rate of order $0.1(1+k)/\eta M_\odot$ yr^{-1}, where η is the efficiency of conversion of mass to kinetic energy.

Part of the work described in this paper has been carried out at the Jet Propulsion Laboratory, California Institute of Technology, under contract with the National Aeronautics and Space Administration. AEW acknowledges support from the NASA Long-Term Space Astrophysics Program. BGP acknowledges helpful conversations with David Meier and helpful comments from the referee, and support from the NASA Summer Faculty Fellowship Program and Whittier College's Newsom Endowment.

REFERENCES

Aller, H. D., Aller, M. F., Hughes, P. A., Wardle, J. F. C., Roberts, D. H., & Homan, D. C. 2001, BAAS, 199, 98.13
Aller, H. D., Aller, M. F., Latimer, G. E., & Hodge, P. E. 1985, ApJS, 59, 513
Attridge, J. M. 2001, ApJ, 553, L31
Ballo, L., et al. 2002, ApJ, 567, 50
Balonek, T., & Kartaltepe, J. S. 2002, BAAS, 200, 17.07
Bicknell, G. V. 1994, ApJ, 422, 542
Blandford, R. D., & Königl, A. 1979, ApJ, 232, 34
Carrara, E. A., Abraham, Z., Unwin, S. C., & Zensus, J. A. 1993, A&A, 279, 83
Celotti, A., & Fabian, A. C. 1993, MNRAS, 264, 228
Celotti, A., Ghisellini, G., & Chiaberge, M. 2001, MNRAS, 321, L1
Cohen, M. H., Cannon, W., Purcell, G. H., Shaffer, D. B., Broderick, J. J., Kellermann, K. I., & Jauncey, D. L. 1971, ApJ, 170, 207
Cotton, W. D., et al. 1979, ApJ, 229, L115
de Pater, I., & Perley, R. A. 1983, ApJ, 273, 64
De Young, D. S. 2002, The Physics of Extragalactic Radio Sources (Chicago:University of Chicago Press)
Dondi, L., & Ghisellini, G. 1995, MNRAS, 273, 583
Ghisellini, G., & Madau, P. 1996, MNRAS, 280, 67
Ghisellini, G., Padovani, P., Celotti, A., & Maraschi, L. 1993, ApJ, 407, 65
Gould, R. J. 1979, A&A, 76, 306
Güijosa, A., & Daly, R. A. 1996, ApJ, 461, 600
Hartman, R. C., et al. 1999, ApJS, 123, 79
Hartman, R. C., et al. 1992, ApJ, 385, L1
Hartman, R. C., et al. 2001a, ApJ, 553, 683 (H01)
Hartman, R. C., et al. 2001b, ApJ, 558, 583
Hartman, R. C., et al. 1996, ApJ, 461, 698
Homan, D. C., & Wardle, J. F. C. 1999, AJ, 118, 1942
Hutter, D. J., & Mufson, S. L. 1986, ApJ, 301, 50
Jones, T. W., & O'Dell, S. L. 1977, A&A, 61, 29
Knight, C. A., et al. 1971, Science, 172, 52
Königl, A. 1981, ApJ, 243, 700
Kubo, H., Takahashi, T., Madejski, G., Tashiro, M., Makino, F., Inoue, S., & Takahara, F. 1998, ApJ, 504, 693
Lähteenmäki, A., & Valtaoja, E. 1999, ApJ, 521, 493
Lähteenmäki, A., Valtaoja, E., & Wiik, K. 1999, ApJ, 511, 112
Leppänen, K. J., Zensus, J. A., & Diamond, P. J. 1995, AJ, 110, 2479
Lister, M. L., Marscher, A. P., & Gear, W. K. 1998, ApJ, 504, 702
Lister, M. L., & Smith, P. S. 2000, ApJ, 541, 66
Mantovani, F., Junor, W., McHardy, I. M., & Valerio, C. 2000, A&A, 354, 497
Maraschi, L., Ghisellini, G., & Celotti, A. 1992, ApJ, 397, L5
Maraschi, L., et al. 1994, ApJ, 435, L91
Marscher, A. P. 1987, in Superluminal Radio Sources, ed. J. A. Zensus & T. J. Pearson (Cambridge:Cambridge Univ. Press), 280
Pearson, T. J. 1995, in Very Long Baseline Interferometry and the VLBA, ed. J. A. Zensus, P. J. Diamond, & P. J. Napier (San Francisco:ASP), 267
Piner, B. G., Edwards, P. G., Wehrle, A. E., Hirabayashi, H., Lovell, J. E. J., & Unwin, S. C. 2000, ApJ, 537, 91
Readhead, A. C. S. 1994, ApJ, 426, 51
Sambruna, R. C. 2000, in Astrophysical Phenomena Revealed by Space VLBI, ed. H. Hirabayashi, P. G. Edwards, & D. W. Murphy (Sagamihara:ISAS), 227
Taylor, G. B. 1998, ApJ, 506, 637
Teräsranta, H., et al. 1998, A&AS, 132, 305
Teräsranta, H., et al. 1992, A&AS, 94, 121
Tingay, S. J., et al. 2001, ApJ, 549, L55
Unwin, S. C., Cohen, M. H., Biretta, J. A., Hodges, M. W., & Zensus, J. A. 1989, ApJ, 340, 117
Unwin, S. C., Wehrle, A. E., Lobanov, A. P., Zensus, J. A., Madejski, G. M., Aller, M. F., & Aller, H. D. 1997, ApJ, 480, 596
Unwin, S. C., Wehrle, A. E., Urry, C. M., Gilmore, D. M., Barton, E. J., Kjerulf, B. C., Zensus, J. A., & Rabaca, C. R. 1994, ApJ, 432, 103
Vermeulen, R. C., & Cohen, M. H. 1994, ApJ, 430, 467
Wehrle, A. E. 1999, Astroparticle Physics, 11, 169
Wehrle, A. E., et al. 1998, ApJ, 497, 178
Wehrle, A. E., Piner, B. G., Unwin, S. C., Zook, A. C., Xu, W., Marscher, A. P., Teräsranta, H., & Valtaoja, E. 2001, ApJS, 133, 297 (Paper I)
Whitney, A. R., et al. 1971, Science, 173, 225